SUPPLEMENTARY MATERIAL to:

Mantle exhumation at magma-poor passive continental margins. Part I. 3D architecture and metasomatic evolution of a fossil exhumed mantle domain (Urdach lherzolite, north-western Pyrenees, France).

by Lagabrielle at al., submitted to BSGF

(full references from Supplementary Material text and plates are displayed in the reference list of the main manuscript)

A. Description of thin sections

1. Microscopic study and mineralogy of the Urdach crust-mantle detachment

Microscopic observation of samples URD1, URD4, URD5 and URD12 confirm that the Urdach lherzolites are locally intensively serpentinized with typical mesh texture and veining development, but that most of the samples preserve relicts of primary minerals (fig. 3supp, Supplementary Material). However, large volumes of the serpentinized mantle underwent by place substantial carbonate veining as well as the complete dissolution of the primary silicates and their replacement by calcite (carbonation). This is well observed in the Bilatre quarry ophicalcite (sample URD1) where the serpentinites along the edges of the calcite veins are fully carbonated (fig. 4supp, Supplementary Material). Some relicts of serpentine mesh are observed a few millimeters away from the veins, as dark, dusty inclusions in calcite. In both URD1 and URD12 samples, the variously

carbonated mantle is dissected by a network of orthogonal sparitic calcite veins with complex crosscutting relationships (fig. 5supp, Supplementary Material).

In hand specimen, sample URD1 exhibits a 3 cm-thick composite vein composed of a core of sheared elongated serpentine leaves separated locally by cataclastic calcite veins (fig. 4supp, Supplementary Material). Thin section observation shows that pervasive carbonation occurred synchronously with calcite veining, in successive stages. Undeformed millimeter wide veins filled with sparitic calcite (veins 1) are crosscut by shear zones centimeter in size paralleling deformed veins (veins 2). Veins 2 are in turn crosscut by undeformed or poorly sheared calcite veins (veins 3). Some calcites display a botryoidal habit in veins showing multi-phased growth. In URD1 sample, co-crystallization of carbonate and serpentine is testified by the occurrence of lenticular flakes of light green serpentine between sparite calcite precipitates. Aggregates of inframillimetric rhomboidal carbonates are included into the serpentine flakes (fig. 4supp D1 and D2, Supplementary Material).

Microscopic study of sample URD12 (fig. 5supp, Supplementary Material) confirms that the serpentinized mantle was affected by pervasive shearing during or after the carbonation. This sample is composed of a part of serpentinized mantle and a part of carbonated mantle. Both parts are cross-cut by numerous shear zones and calcite veins. At the microscopic scale, the carbonated mantle exhibits a foliation defined by parallel shear zones with calcite grain reduction. This foliation parallels the limit between the carbonated and the non-carbonated mantle, which also appears as a main shear zone (fig. 5supp A and B, Supplementary Material).

Finally, the mesoscopic and microscopic observations of ultramafic samples from the Bilatre quarry collectively reveal that the Urdach ophicalcites have recorded a complex history of syn-tectonic mantle carbonation.

Based on thin section observation, the albitite-like sample URD9-1 is quartz-free and composed of large and fully sericitized inframillimetric feldspars surrounded by dominant, equigranular millimetric albite crystals. It exhibits numerous well-crystallized zircons (hundreds of microns in size), like the albitite dikes described by Pin et al. (2001, 2006). Millimeter-wide shear zones exhibiting cataclastic albites in a groundmass of very small muscovites (sericite) cross-cut the sample (fig. 6supp A1 and 7supp, Supplementary Material). Electron-probe microanalyses were performed on various muscovite, albite and 30 zircons from this sample (table 4, Supplementary Material). Meter-wide veins sampled close to the albitite-like URD9-1 are made of green chlorite flakes forming large rosettes associated with large hydrothermal quartz crystals hosting numerous fluid inclusions (samples URD9-2: fig. 7supp C, Supplementary Material and samples URD9-b and URD9-f, microscopic view not shown). These chlorite-rich veins display quartzose borders showing two generations of quartz: the first one consists of large crystals, the second one is composed of small crystals in geodic cavities (sample URD9-c, microscopic view not shown). Shear zones in which the chlorites are fragmented and recrystallized in small crystals cross-cut the entire samples. Microprobe analyses indicate that samples URD9-b, URD9-c and URD9-f are Cr-muscovite-rich (fuchsite) together with various amount of quartz, clinochlore and rutile (table 5, 6, 7, Supplementary Material). This Cr-rich mineralogical association has affinity with listvenite assemblages (see more details in subsection 2 below).

Large millimetric flakes of dark green static chlorite, often arranged in rosettes, are the dominant component of the chloritite from the Urdach breccia (sample BCOR115), together with numerous zircons of hundreds of microns across (fig. 7supp D, Supplementary Material). This rock is devoid of any deformation. It may derive from the disaggregation of either a metasomatic chlorite vein from the crust-mantle detachment

77 similar to veins in samples URD9-2 or of the border of an albitite dike intrusive in the
78 mantle rocks. Electron-probe microanalyses were performed on on 12 chlorites and 7
79 zircons from this sample (table 8, Supplementary Material). By contrast with the chlorites
80 from the Saraillé crust-mantle detachment and cover décollement, these Mg-chlorites
81 (clinochlore) are Cr-free. The BCOR115 zircons were dated by in situ U/Pb LA-ICP-MS
82 (see section V and fig. 6supp, Supplementary Material).
83
84 2. Microscopic study and mineralogy of the Urdach cover décollement: evidence for
85 metasomatic transformations
86 As shown by the observation of sample URD17b (sub-unit a) thin section, the lherzolites
87 lying against the Urdach cover décollement, north-east of Col d'Urdach, are deeply
88 serpentinized with well-developed mesh textures and limited marks of pervasive
89 carbonation (fig. 8 B). Most pyroxenes are changed to bastite with rare cores containing
90 relics of fresh minerals. Small spinels are widespread in the groundmass. A rough tectonic
91 fabric is marked by the flattening of the serpentinized olivine that parallel the dark septae
92 of the mesh texture. Some calcite-rich fractures cross-cut the lherzolites. Mineral
93 microprobe analyses of sample URD17b reveal the presence of relict cpx and
94 metamorphic phases such as Cr-rich clinochlore and magnesian amphiboles replacing
95 pyroxenes (table 9, Supplementary Material). The mesh texture groundmass is composed
96 of pseudomorphic serpentines whose SiO_2 and MgO contents vary between 39 and 45
97 wt%, and 27 and 31 wt % respectively. Their FeO tot content ranges from 5 to 8% and
98 they contain a rather high amount of Al (Al_2O_3 = 6 to 8 %). Apart from the Al content,
99 these compositions fall in the range of compositions of serpentines from oceanic or
100 ophiolitic environments. We provide hereafter some compositions for reference. In the
101 serpentine from the Iberia margin, SiO_2 content varies between 38 and 42 wt% and MgO

content varies between 28 and 38 wt%; FeO content ranges from 4 to 7 wt% (Agrinier et al., 1988). In the ophiolitic Chenaillet serpentinites (French western Alps), SiO_2 and MgO contents vary between 44 and 38 wt %, and 43 and 34 wt % respectively and FeO content ranges from 2 to 9 wt % (Lafay et al., 2017). The FeO content ranges from 2 to 8 wt% and may reach 12 wt % in serpentine from mesh textures of the South West Indian Ridge (Rouméjon et al., 2015). It ranges from 1.3 to 6.9 wt % in serpentine from ophiolites in Mexico (Gonzalez-Mancera et al., 2009), and may reach up to 19% wt % in chrysotile from Quebec (Faust and Fahey, 1962). This comparison points to a rather high Al_2O_3 content of the Col d'Urdach serpentine compared to the composition of serpentines from the Indian Ridge and from the Chenaillet (Al_2O_3 content between 0.9 and 4 wt % and 0.2 to 3.4 wt % respectively). This high content most likely records the presence of bastitized cpx as already reported by Agrinier et al., (1988) who studied composition variations of hydrated minerals in the Iberia margin mantle. Here, high Al_2O_3 content (up to 5.38 wt %) are found in serpentine after orthopyroxene whereas serpentine from olivine are almost Al-free. Alternatively Padrón-Navarta et al., (2013) have shown that Al-content in natural antigorite changes substantially as a function of pressure and temperature in response to Tschermak's exchange in antigorite solid solution. A higher Al-content being favored at lower pressure and higher temperature. Note that serpentine may incorporate high contents of Al as shown by analyses of metasomatic komatiite (Al_2O_3 content max 15.8 %, Albino, 1995) indicating that the Urdach compositions are not uncommon.

Thin section observation of the vein-textured metasomatic assemblages from the Urdach cover décollement (sample URD17a, sub-unit b) reveals an intimate intergrowth of fibrous calcite and serpentine (fig. 8supp F in Supplementary Material). Two different generations of serpentine can be distinguished owing to the habitus of the fiber

127 intergrowths. Ante- to syn-deformation serpentine are sheared and tightly folded in the
128 intercept of conjugate shear zones whereas another serpentine generation corresponds
129 to acicular post-kinematic crystals. These microtextural relationships indicate that
130 serpentine growth occurred synchronously with the calcite crystallization (with minor
131 edenite), during and after faulting activity along the Urdach cover décollement. Sample
132 URD17a serpentines have SiO_2 content between 42 and 45% and MgO content between
133 32 and 35%. They have low relatively Al and Fe content (FeO and Al_2O_3 contents between
134 5 and 8% and between 2 and 3%, respectively: table 10, Supplementary Material),
135 compared to the in-situ pseudomorphic serpentines from the massive lherzolite of sub-
136 unit a (sample URD17b). These relatively low Fe and Al contents are consistent with their
137 occurrence in veins as fluid precipitates. Dolomite was not found in this vein system.
138 Indeed, microanalyses of fifteen carbonate crystals from sample URD17a reveal that only
139 calcite crystallized together with serpentine in this deforming zone, close to the mantle
140 body (table 10, Supplementary Material). Still in sub-unit b, the carbonates forming the
141 large veins situated less than one meter to the north of the cover décollement fault
142 (sample URD16, fig. 10) display both syn- and post-kinematic characters. Under the
143 microscope, static assemblages are composed of aggregates of carbonates isolating
144 millimetric areas filled with small chlorite flakes devoid of preferred orientation, and
145 locally arranged in small, contiguous rosettes (fig. 8supp E, Supplementary Material).
146 Brownish areas rich in truncated clusters of millimeter-sized opaque grains probably
147 correspond to relict of mesh texture. This would imply that totally carbonated lherzolite
148 clasts were incorporated in carbonate veins situated some meters away from the Urdach
149 mantle. Surprisingly, sample URD16 static chlorites are mostly Cr-poor clinochlores
150 (Cr_2O_3 content between 0.02 and 0.79 %; SiO_2 content between 32 and 34%; MgO
151 content between 28 and 30%, table 11, Supplementary Material) indicating a post-

deformational fluid source devoid of ultramafic influence. The sigmoidal lenses alternating with the calcite veins are all cataclastic carbonate breccias with numerous evidence of hydrofracturing brecciation as shown by microscopic study of sample URD13 texture (fig. 8supp A, Supplementary Material). These cataclastic carbonates derive from a fully recrystallized sedimentary protolith, a Liassic limestone belonging to the basal layers of the Mail Arrouy pre-rift sequence as indicated by the BRGM geological map (Casteras et al., 1970). These brecciated limestones also contain chlorite aggregates that have crystallized together with calcites, accounting for important fluid circulation in the sigmoidal lenses of metasediments associated with veins. According to microprobe analyses, URD13 chlorites are also clinochlores with variable but relatively low Cr_2O_3 content (0.9 wt % max) (table 12, Supplementary Material). This confirms some chemical transfers from mantle rocks by means of fluid exchange along the cover décollement.

The cores of the orange-colored dolomitic lenses of sub-unit c (samples URD18 : fig. 8supp in Supplementary Material) and URD20 (not shown), consist of a tectonic microbreccia showing angular clasts of recrystallized dolomitic material separated by veins entirely composed of euhedral micro-dolomites. We performed electron probe micro-analyses of eighteen dolomitic crystals from sample URD18 in order to detect heterogeneities between clasts and cement (table 13, Supplementary Material). A striking feature here is the high level of recrystallization of the entire dolostone as shown by the presence of large euhedral crystals. MgO and CaO concentrations are comprised between 20 - 22% and 31 - 32%, respectively. We found only trace amounts of Cr and Ni and less than 1.38% FeO. The homogeneous composition of both clasts and their host veins argues for a closed fluid system during deformation.

Sample URD14 (sub-unit c) is a black marble crossed-cut by numerous white calcite veins at the hand specimen scale. Thin section observation also reveals a tight micro-veining,

177 orthogonal to a schistosity marked by the flattening of carbonate beds rich in bioclasts
178 and deformed microfossils (fig. 10 C). The fossiliferous beds contain abundant
179 foraminiferas, mostly *Miliolidae*, representative of Liassic platform environments (J.
180 Canérot, pers. comm.). Sample URD14 is also marked by the presence of numerous pyrite
181 crystals. Microprobe analyses indicate that the carbonates are mostly calcite and confirm
182 the occurrence of pyrite (table 14, Supplementary Material). It is worth noting that a
183 RSCM temperature of 300°C was obtained for sample URD14 (Corre et al., in prep.).
184 Samples URD19 and URD15 located 30 m away from the cover décollement fault in sub-
185 unit d (fig. 10 A2 and D), display peculiar aspects and compositions. URD19 is a dolomitic
186 breccia with recrystallized geodic dolomites (fig. 8supp H and I, Supplementary Material).
187 Microprobe analyses show that large calcite crystals are associated with dolomite in the
188 veins, with rare white mica (table 15, Supplementary Material). Dolomite contain small
189 amounts of FeOtot (up to 3.4%). The veins are filled with an assemblage of opaque
190 minerals including sphalerite and pyrite associated with possible pyrrhotite (FeO =
191 62.18%) (fig. 8supp I, Supplementary Material). Thin section observation of sample
192 URD15 (fig. 8supp C, Supplementary Material) reveals the presence of large areas of
193 micro-calcite that contain striated zones of a dusty black material (not shown). These
194 dark areas represent ghosts of fully carbonated pyroxenes and relicts of mesh textures,
195 thus confirming their origin from a deeply transformed mantle protolith. Calcites contain
196 trace amounts of Fe (0.5% FeO). They are associated with rare dolomite containing some
197 amount of Fe (FeO=2.3%) (table 16, Supplementary Material). Small aggregates of quartz
198 crystals are associated with the calcites. The rock is cross-cut by shear bands associated
199 with a rough foliation and are composed of a carbonated ultramafic material with relicts
200 of pyroxenes, well observed in some large calcite crystals. Flakes of partially sheared
201 green pleochroic mica crystallized in the deformed bands (fig. 8supp C, Supplementary

202 Material). They contain 22-26% Al_2O_3, 6-9% K_2O, 3-4% MgO, 0-2% NiO and 2-7% Cr_2O_3
203 (on the basis of fourteen microprobe analysis: table 16, Supplementary Material). These
204 Cr-rich white micas are Cr-muscovite (fuchsite), a mineral frequently encountered in
205 ultramafic environments. The association of calcite, quartz, Cr-muscovite and accessory
206 chlorite in metasomatic zones on the site of former ultramafic material defines the rock-
207 type listvenite (e.g. Buisson and Leblanc, 1986). Listvenites often contain additional
208 serpentine, talc and chlorites. The formation of listvenites is linked to carbonation and
209 silicification by CO_2-rich fluids that circulate through intensively sheared peridotites
210 (Harlov and Austrheim, 2013, with references therein). In addition, it must be noticed
211 that URD15 is largely invaded by pyrite that crystallized in grains up to some mm wide
212 (fig. 10 D). Carbonation and silicification implies the circulation of a great amount of
213 fluids able to dissolve the mantle silicates and to precipitate the carbonates and the
214 quartz. However, while listvenitization exert a fundamental change in rock texture and
215 mineralogy, it has been shown that, with the exception of volatiles, the primary ultramafic
216 rock composition (e.g content in MgO + CaO/SiO_2) can be preserved (Falk and Kelemen,
217 2015). The occurrence of listvenite implies that a tectonic slice of deeply metasomatized
218 mantle rocks is present here. Due to poor exposure conditions, it is not possible to
219 precise the structural position of this mantle unit. It is probably thrusted over the
220 tectonic lenses of Mesozoic carbonates due to a local reverse fault as represented in
221 figure 10.
222 Our knowledge of the metasomatic mineralogical assemblages from the Urdach cover
223 décollement is completed by the analysis of the Peillou section rock suite. Sample
224 BCOR300a consists of submillimetric albite crystals with diffuse margins containing
225 patches of thinly crystallized sericite. The largest albite crystals are surrounded by a
226 chlorite-rich groundmass that contains large millimetric euhedral zoned zircons (fig. 8 J,

227 Supplementary Material). Locally, shear bands with small euhedral albites and micas
228 cross-cut the thin section. The chlorites of sample BCOR300a are either Mg- or Fe-rich,
229 Cr-free clinochlores (MgO = 30 to 17 wt% and FeO Tot = 17 to 5 wt%) (table 17,
230 Supplementary Material) similar to those of sample BCOR115. The analyzed micas are
231 muscovite. This zircon-bearing albitite has an unclear structural position like sample
232 URD9-1 albitite. It probably represents a former dike, intrusive into the Urdach mantle,
233 that was exposed close to the seafloor during mantle exhumation and that was later
234 incorporated into the Peillou complex fault zone as the result of the Pyrenean
235 compressional tectonics.
236 In thin section, sample BCOR300b is dominated by the intergrowth of large talc and
237 chlorite crystals (fig. 8supp K, Supplementary Material). The chlorites are Cr-rich, Mg-
238 clinochlores (Cr_2O_3 content = 0.3 to 1.4 wt% based on six analyses: table 18,
239 Supplementary Material). Such an association of talc and Cr-rich chlorite is also largely
240 present in the Saraillé massif (see companion paper, Lagabrielle et al., submitted). This
241 talc-chlorite association thus appears as an important characteristic of the contact zones
242 between mantle rocks and the hanging wall material, whatever the latter could be. As a
243 consequence, rock-type BCOR300b can be regarded as an equivalent of the metasomatic
244 pink talcschists exposed along the cover décollement of the Saraillé massif (e.g. sample
245 BCOR30) (see companion paper, Lagabrielle et al., submitted).
246 Sample BCOR300c (fig. 9supp, Supplementary Material) comes from a tectonic breccia
247 that incorporates clasts of various origin. Most of them derive from Triassic protoliths,
248 such as brecciated and foliated orange dolostones and minor meta-ophites. Microprobe
249 analyses confirm the presence of largely recrystallized dolomite (some of them are iron-
250 rich) and of albite that replaces the plagioclase microliths in a meta-ophite clast (table 19,
251 Supplementary Material). The meta-evaporite BCOR300e is mostly composed of small

interpenetrated anhydrite crystals (microprobe identification of S) with minor inclusions of euhedral calcites and dolomites and a small amount of newly formed quartz (table 20, Supplementary Material).

B. LA-ICP-MS U-Pb dating of zircons

U-Pb geochronology of zircon was conducted in-context (i.e. in thin-sections) by in-situ Laser Ablation - Inductively Coupled Plasma - Mass Spectrometry (LA-ICP-MS) at Géosciences Rennes using an ESI NWR193UC Excimer laser coupled to a quadripole Agilent 7700x ICP-MS. During the course of an analysis, the signals of ^{204}(Pb+Hg), ^{206}Pb, ^{207}Pb, ^{208}Pb, ^{232}Th and ^{238}U masses are acquired. No common Pb correction was applied owing to the large isobaric interference with Hg. The ^{235}U signal is calculated from ^{238}U on the basis of the ratio ^{238}U/^{235}U=137.88. For more information on the analytical protocol and the settings of the instruments, see Ballouard et al. (2015) as well as table 2 in Supplementary Material. Data were corrected for U–Pb and Th–Pb fractionation and for the mass bias by standard bracketing with repeated measurements of the GJ1 zircon standard (Jackson et al., 2004). Repeated analyses of the Plešovice zircon standard (Sláma et al., 2008) treated as unknown were used to control the reproducibility and accuracy of the corrections (see table 2 in Supplementary Material) and yield a concordia age of 337.7 ± 3.6 Ma (MSWD=0.54, N=9). Data reduction was carried out with the GLITTER® software package developed by the Macquarie Research Ltd. (Van Achterbergh et al., 2001). Concordia diagrams were generated using Isoplot/Ex (Ludwig, 2001). All errors given in table 3 in Supplementary Material are listed at one sigma, but where data are combined to calculate an age, the final results are provided with 95% confidence limits.

In context zircon U/Pb dating of a sericite-albitite in contact with the Urdach mantle rocks: sample URD9-1

Zircon grains are generally big in size (0.5-1.5mm) and characterized by a relatively homogeneous center surrounded by lighter concentric zoning (Fig. 6supp A, Supplementary Material). Thirty-four analyses out of 7 large zircon grains were performed directly in thin section (table 3 in Supplementary Material). The common Pb contents are usually low (f206% between 0 and 4.7%). These zircon grains have very variable Th, U and Pb contents (114-9816 ppm, 46-573 ppm and 1-57 ppm respectively) yielding high and variable Th/U ratios (2 to 33). Unusually high Th/U ratios have already been described in some zircon grains from carbonatite and nepheline syenite pegmatite (up to 1000; Belousova et al., 2002).

In a Tera-Wasserburg diagram (Fig. 6supp B Supplementary Material) the data plot in a discordant to concordant position (depending on their common Pb contents). Seven concordant analyses within error yield a Concordia date of 112.9 ± 1.6 Ma (Fig. 6supp B inset, Supplementary Material). The positions of the remaining data are interpreted as the consequence of the presence of common Pb and/or a slight Pb loss. The mean $^{206}Pb/^{238}U$ date for all the data but one is equivalent within error at 111.7 ± 0.8 Ma (MSWD=2.7; Fig. 6supp C, Supplementary Material).

In context zircon U/Pb dating of a clast of static chloritite from the Urdach breccia: sample BCOR115

Zircon grains are generally large (0.5 mm) and characterized, in cathodoluminescence, by some grains with rather homogeneous dark-cores surrounded by concentric lighter zonings (Fig. 6supp D Supplementary Material) while others are homogeneous with a very faint luminescence. Twenty-nine analyses out of 8 zircon grains were performed in

thin-section (table 3 in Supplementary Material). In some of the analyzed grains, the common Pb contents can be very high (f206% up to 57%). Analyses are variable in terms of Th, U and Pb contents (311-19413 ppm, 14-1104 ppm and 2-122 ppm respectively). These zircon grains also yield highly variable albeit very high Th/U ratios (4-35). Plotted in a Tera-Wasserburg diagram (Fig. 6supp E, Supplementary Material), the data are sub-concordant to discordant and yield a lower intercept date of 109.4 ± 1.2 Ma (MSWD=2.7). If the isochron is forced to the common Pb composition at ca. 110 Ma according to Stacey and Kramers' model (1975), we obtain a similar date of 110 ± 1.2 Ma (MSWD = 3.2, not shown).

Captions to figures and photographic plates of Supplementary Material.

Figure 1supp. Field aspects of the Urdach breccia and views from the Mer de Her area.

A: a clast of poorly sheared andalusite schist rarely observed in the Urdach breccia (close to Soum d'Ombrets). B: mylonitic gneiss very frequently observed in the Urdach breccia. C: high angle dipping of the foliation in the lens of Paleozoic material (Silurian?) welded on the Urdach mantle at Mer de Her. D, E, F: various aspects of the breccia in the Mer de Her area. Breccia is welded by a quartz-rich cement containing by place abundant concentrates of iron oxides (D and F); it suffered local dissolution (cellular aspect due to vacuolar quartz cement, D). The clasts are mostly mylonitic quartzites. G: tectonic breccia found as a clast in the Urdach breccia close to Soum d'Ombrets. It is composed of clasts from a mylonitic micaschist. Some of the clasts underwent very little relative displacement.

Figure 2supp. Deformation and fluid-rock interactions in the Mesozoic cover above the Urdach cover décollement.

A: lenticular fabric and conjugate shear zones in the Jurassic marbles exposed along the trail to Soum de Ségu (cover décollement at hill 488). B: calcite veining (Granges Lacues). C: N-S vertical schistosity in the Jurassic marbles exposed some meters beneath the trail to Soum de Ségu (cover décollement at hill 488). D: foliated tectonic breccia (clast boudaries are outlined by conjugate shear planes).

Figure 3supp. Microscopic view of the serpentinized Urdach mantle (sample URD4).

Serpentinizaton is not complete and relic olivines and pyroxenes are still visible through the pervasive serpentine mesh texture.

Figure 4supp. The Bilatre quarry ophicalcites: sample URD1, hand specimen and microscopic aspects.

A1: photograph of hand specimen. A2: structural interpretation. The sample shows a 3 centimeters thick shear zone with light serpentine fibers and calcite intergrowths, defining a curved foliation (f). At least 3 generations of calcite veining can be identified. Veins 1 may have developed before the shearing event, veins 2 are emplaced during the shearing event and veins 3 crosscut f. B: microscopic view of vein 2 showing sheared serpentine and calcite. C: microscopic view of veins 1 and 2 relationships. D1 and D2: close up on microscopic evidence for co-genetic relationships between serpentine in veins and carbonates (most probably calcite) (serp. = serpentine).

Figure 5supp. The Bilatre quarry ophicalcites: sample URD12, hand specimen and microscopic aspects.

A: photograph of hand specimen and its structural interpretation. The sample shows a large portion of carbonated mantle (light blue) crosscut by few calcite veins. B: microscopic view (location in A) showing the transition from the serpentinized mantle (green) to the fully carbonated area. This transition corresponds to numerous shear zones affecting both carbonates and serpentine minerals in the serpentinzed mantle. A shear zone marks the sharp boundary with the fully carbonated mantle. This shear zone might be syn- or post-carbonation. C and D: detailed microscopic views showing evidence for the development of syn-carbonation shear zones (carb. = carbonated, serp. = serpentine, lherz. = lherzolite, amphi = amphibole, cpx = clinopyroxene).

Figure 6supp. In situ U/Pb zircon dating.

A1: microscopic view of sample URD9-1. A2: cathodoluminescence picture of a typical zircon grain from sample URD9-1. B: Tera-Wasserburg diagram for sample

URD9-1 (inset shows the concordia age). C: mean $^{206}Pb/^{238}U$ date obtained from the zircon analyses (sample URD9-1). D1: microscopic view of sample BCOR115. D2: cathodoluminescence picture of a typical zircon grain from sample BCOR115. E: Terra-Wasserburg diagram for sample BCO115.

Figure 7supp. Metasomatic rocks of the crust-mantle detachment.

A, B and D: microphotographs of the dated samples URD9-1 and BCOR115. C: microphotograph of the chlorite-schist URD9-2 containing Cr-muscovite (alb = albite, zr = zircon, chl = chlorite, Cr-ms = Cr-muscovite : fuchsite).

Figure 8supp. Microphotograph of the main rock-types composing the cover décollement fault rocks along (i) the "ball trap" (A to I, location of samples in fig. 10) and (ii) the Peillou sections (J, K, L).

A: URD13, hydrofractured dolostone. B: URD14, sheared fossiliferous black limestone. C: URD15, listvenite. D, E and F: calcite veins with static chlorites and possible relict of mesh texture (carbonated mantle rock?) (URD16) or deformed and non deformed serpentine sheets (URD17a). G: URD18: monomictic dolostone tectonic breccia (dol = dolomite). H and I: URD19, dolostone breccia with calcite veining (calc) and sphalerite (sphal.). J, K and L: rocks from the Peillou section. Zircon-bearing albitite (BCOR300a), chlorite-talc-schist (BCOR300b), meta-evaporite (anhydrite, BCOR300e).

Figure 9supp. Triassic tectonic breccia at Peillou: sample BCOR300c.

A: microscopic view (natural light) showing a millimeter-sized clast of meta-ophite in a groundmass of dolostone micro-breccia. B: BSE image of the meta-ophite clast shown in A with the location of analyzed albites (points 56 to 61). C: additionnal

382 microscopic view showing various clasts in the same groundmass of dolostone
383 micro-breccia (dol. = dolomite).

384 Figure 10supp. Lavas in the Late Albian flysch at Bilatre : macroscopic aspects.

385 A, B, C: illustration of the altered and non altered spherulitic facies. D, E: flysch
386 inclusions in the lavas.

387 Figure 11supp. Lavas in the Late Albian flysch at Bilatre : microscopic aspects.

388 A: sample BCOR394, contact between flysch sediments and fresh lava. B: sample
389 BCOR274. Typical spherulitic texture. Note flattening of spherulites along the doted
390 white line (syn- or post-emplacement). C: close up of hyaloclastite fragment. D: a
391 millimeter-sized clast from a massive lava fragment with radial microlitic texture. E:
392 details of quartz fragments (note the presence of both euhedral crystals and
393 polycrystalline aggregates). F: typical poorly deformed spherulitic texture.

394

395 Table 1. Major and trace element analysis of handpicked glassy spherulites from Bilatre
396 (sample BCOR394d). Major elements as oxides wt%, trace elements in ppm. Total
397 iron as Fe_2O_3; LOI: Loss On Ignition at 1050°C. ICP-AES data, Plouzané. Analytical
398 methods described in Cotten et al. (1995).

399

400 Table 2. Operating conditions for the LA-ICP-MS equipment.

401

402 Table 3. U-Th-Pb data obtained on zircon grains by LA-ICP-MS

403 All errors are reported at 1 sigma. For sample URD9-1, data in bold were used to
404 calculate the concordia age. Concordance was estimated as Conc% = (Age
405 ($^{206}Pb/^{238}U$) x 100)/(Age($^{207}Pb/^{235}U$)) f206% = ($^{207}Pb/^{206}Pb_m$ -
406 $^{207}Pb/^{206}Pb^*$)/($^{207}Pb/^{206}Pb_c$-$^{207}Pb/^{206}Pb^*$)x100

Tables 4 to 20. Microprobe mineralogical analyses.

Analytical techniques. The chemical compositions of minerals was acquired by microprobe analysis on five samples and are listed in tables 1 to 5. The major-element compositions of the minerals were determined by electron microprobe analysis using a CAMECA SX100 at Service Commun de Microsonde Ouest (SCMO), Plouzané, France. using a CAMECA SX100 microprobe, operated at 15 kV, 20nA, spot size 5 µm and 10 s counting time on peak and 5 s on background. The EPMA instrument was equipped with five WDS detectors with LIF, PET, and TAP crystals, and all elements were assigned to specific detectors to be measured 5 + 5 concurrently per run of ~ 30 s total duration. Standards were natural albite (Na, Si), orthoclase (K), corundum (Al), wollastonite (Ca), forsterite (Mg), $MnTiO_3$ (Mn, Ti), andradite (Fe) and chromite (Cr). Raw spectral data were ZAF-corrected using the phi-rho-Z protocol of Pouchou and Pichoir (1984) known as 'PAP'. Element contents were recalculated to oxides by stoichiometry, total iron content is represented as FeO. Limits of detection are: 0.01 wt% (Mn, Ti, Fe, Cr), 0.05 wt% (Ca, Si, K) and 0.10 wt% (Al, Mg, Na). Main element oxide contents in wt% were recalculated into mineral compositions in atoms per formula unit – apfu using standard routines. Volatiles contents in H_2O and/or CO_2 were calculated by balance of the sum total with 100.00 wt%. Mineral names are abbreviated according to recommendations by Whitney and Evans (2010).

Table 4: Microprobe mineralogical analyses, sample URD9-1

Table 5: Microprobe mineralogical analyses, sample URD9b

Table 6: Microprobe mineralogical analyses, sample URD9c

Table 7: Microprobe mineralogical analyses, sample URD9f

Table 8: Microprobe mineralogical analyses, sample BCOR115

Table 9: Microprobe mineralogical analyses, sample URD17b

Table 10: Microprobe mineralogical analyses, sample URD17a

Table 11: Microprobe mineralogical analyses, sample URD16

Table 12: Microprobe mineralogical analyses, sample URD13

Table 13: Microprobe mineralogical analyses, sample URD18

Table 14: Microprobe mineralogical analyses, sample URD14

Table 15: Microprobe mineralogical analyses, sample URD19

Table 16: Microprobe mineralogical analyses, sample URD15

Table 17: Microprobe mineralogical analyses, sample BCOR300a

Table 18: Microprobe mineralogical analyses, sample BCOR300b

Table 19: Microprobe mineralogical analyses, sample BCOR300c

Table 20: Microprobe mineralogical analyses, sample BCOR300e

Légende des figures et tableaux supplémentaires.

Figure 1supp. La brèche d'Urdach, aspects de terrain et vues sur Mer de Her.

Figure 2supp. Déformation et interactions fluide-roche dans la couverture mésozoïque au dessus du décollement de couverture d'Urdach.

Figure 3supp. Le manteau serpentinisé d'Urdach (échantillon URD4) : aspect microscopique.

Figure 4supp. Les ophicalcites de la carrière de Bilatre (échantillon URD1).

Figure 5supp. Les ophicalcites de la carrière de Bilatre (échantillon URD12).

Figure 6supp. Datations U/Pb in situ sur zircons.

Figure 7supp. Les roches métasomatiques du détachment croûte-manteau.

Figure 8supp. Les roches métasomatiques du décollement de couverture (« ball trap » et Peillou.

Figure 9supp. Les brèches tectoniques triasiques de Peillou: échantillon BCOR300c.

Figure 10supp. Les laves dans le flysch de Bilatre : aspects macroscopiques.

Figure 11supp. Les laves dans le flysch de Bilatre : aspects microscopiques

Tableau 1. Analyse des éléments majeurs et des traces de l'échantillon de lave sphérulitique BCOR394d (oxydes wt% et ppm; fer total en Fe_2O_3, LOI (Loss On Ignition): perte au feu à 1050°C. données ICP-AES, Plouzané. Méthode analytique décrite dans Cotten et al. (1995).

Tableau 2. Conditions opératoires pour le fonctionnement de l'équipement LA-ICP-MS.

Tableau 3. Données U-Th-Pb obtenues sur grains de zircon par LA-ICP-MS

Tableaux 4 à 20. Analyses de minéraux à la microsonde.

Tableau 4: Analyses de minéraux à la microsonde de l'échantillon URD9-1

Tableau 5: Analyses de minéraux à la microsonde de l'échantillon URD9b

Tableau 6: Analyses de minéraux à la microsonde de l'échantillon URD9c

Tableau 7: Analyses de minéraux à la microsonde de l'échantillon URD9f

Tableau 8: Analyses de minéraux à la microsonde de l'échantillon BCOR115

Tableau 9: Analyses de minéraux à la microsonde de l'échantillon URD17b

Tableau 10: Analyses de minéraux à la microsonde de l'échantillon URD17a

Tableau 11: Analyses de minéraux à la microsonde de l'échantillon URD16

Tableau 12: Analyses de minéraux à la microsonde de l'échantillon URD13

Tableau 13: Analyses de minéraux à la microsonde de l'échantillon URD18

Tableau 14: Analyses de minéraux à la microsonde de l'échantillon URD14

Tableau 15: Analyses de minéraux à la microsonde de l'échantillon URD19

Tableau 16: Analyses de minéraux à la microsonde de l'échantillon URD15

Tableau 17: Analyses de minéraux à la microsonde de l'échantillon BCOR300a

Tableau 18: Analyses de minéraux à la microsonde de l'échantillon BCOR300b

Tableau 19: Analyses de minéraux à la microsonde de l'échantillon BCOR300c

Tableau 20: Analyses de minéraux à la microsonde de l'échantillon BCOR300e

Figures du texte principal

Figure 1. Carte simplifiée de la chaîne Pyrénéo-cantabrique et localisation de la zone étudiée (modifiée d'après Teixell et al., 2018).

Figure 2. Carte géologique des « Chainons Béarnais » (Corre, 2017) et situation des massifs du Saraillé et d'Urdach.

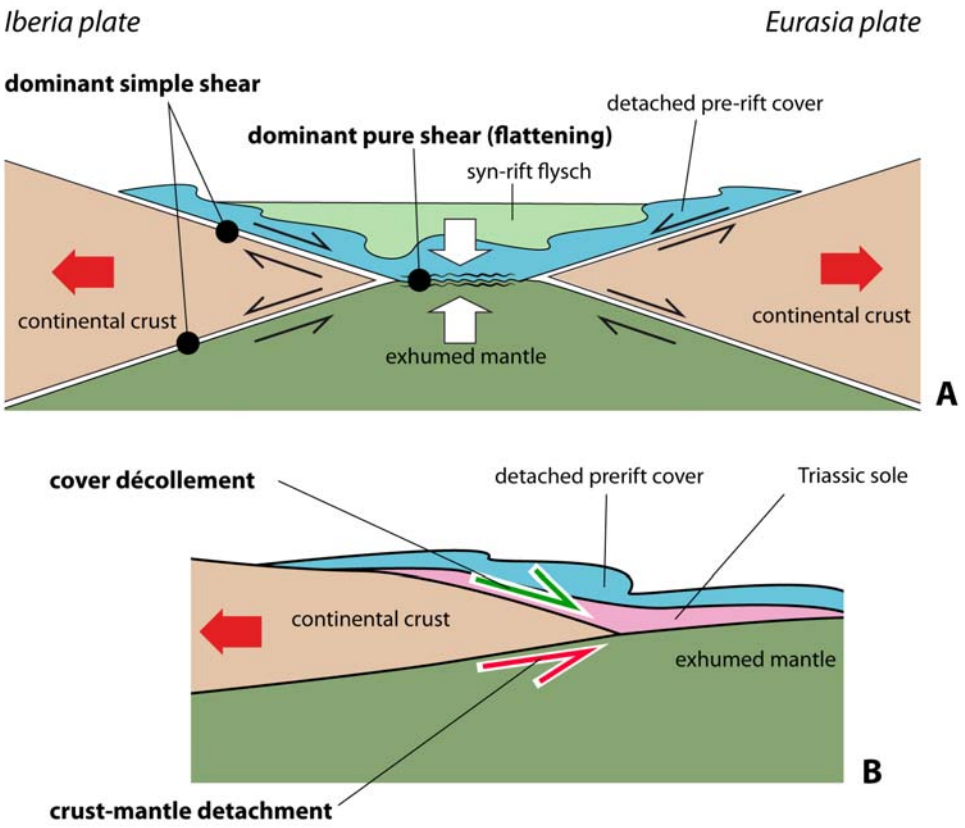

fig.3-URD

Figure 3. Schémas des éléments tectoniques caractéristiques dans une marge passive distale à manteau exhumé. A: répartition des modes de déformation en cisaillements simple et pur; B: position du détachement croûte-manteau et du décollement de couverture dans la marge distale.

Figure 4. Carte détaillée du massif d'Urdach (Corre, 2017) et coupe a-b. Stéréogrammes A1, A2, B, C et D repérés sur la carte.

Figure 5. Photographies montrant quelques aspects typiques des brèches d'Urdach.

Figure 6. Vue panoramique sur le Col d'Urdach depuis Soum d'Unars. On regarde vers le NE.

Figure 7. La zone lenticulaire du détachement croûte-manteau au Col d'Urdach et à Bilatre (vues de terrain).

Figure 8. Les ophicalcites du Col d'Urdach et de Bilatre (vues de terrain et aspects microscopiques).

Figure 9. Les roches métasomatiques sur le site de l'échantillon URD9-1 (vues de terrain).

Figure 10. Le décollement de couverture au site du "ball trap".

Figure 11. Reconstruction en 3D du plancher d'un bassin crétacé de la ZNP d'après la géologie du site d'Urdach (modifié d'après Corre, 2017).

518 Figure 12. Les interactions entre le détachement croûte-manteau et le décollement de

519 couverture dans la marge distale nord-ibérique.

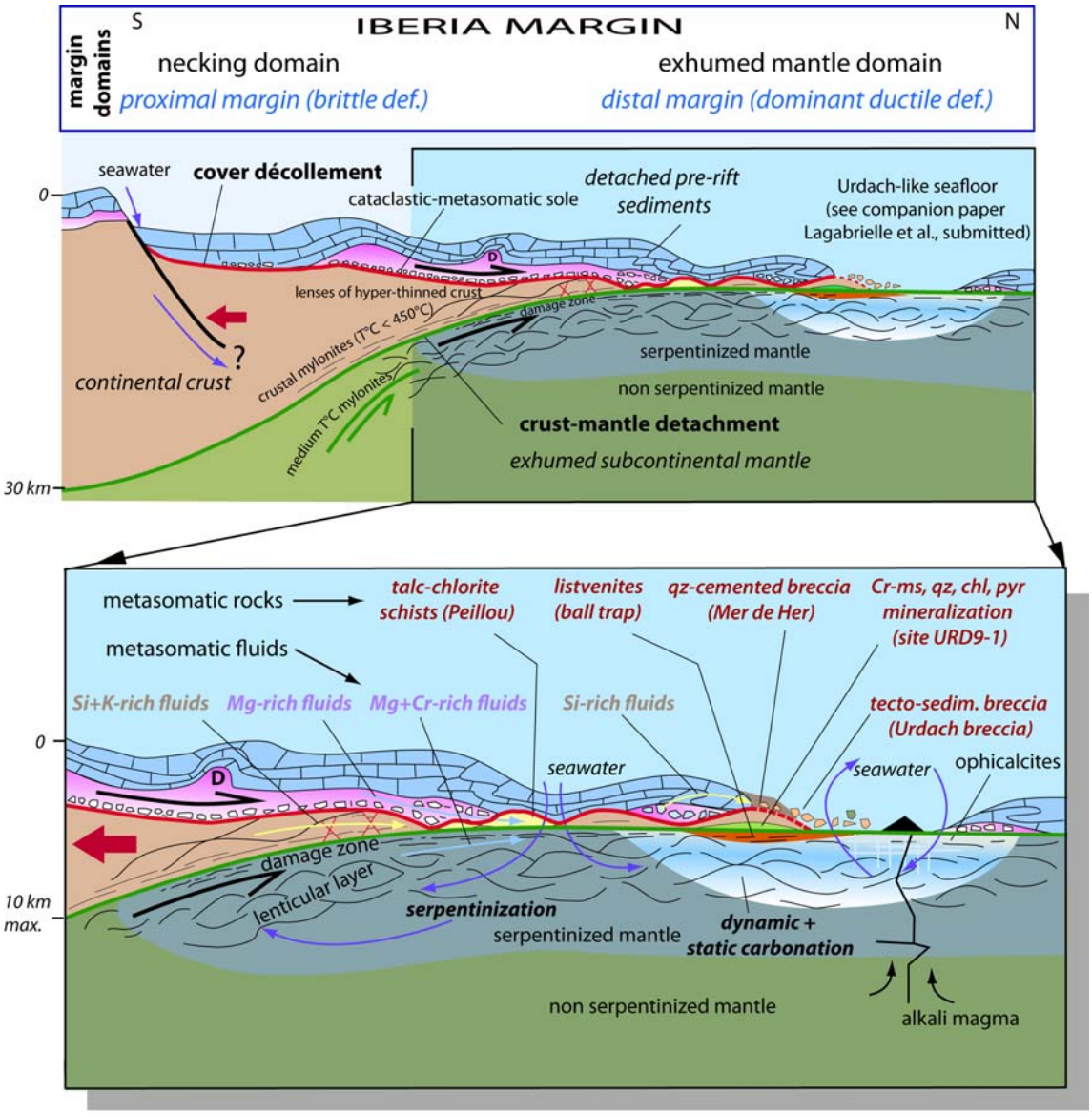

520

521 Figure 13. Architecture de la marge nord-ibérique et schéma de la circulation des fluides

522 associée au fonctionnement des grands détachements.

523

524

Matériel supplémentaire : figures et tableaux

Figure 1supp. La brèche d'Urdach, aspects de terrain et vues sur Mer de Her.

Figure 2supp. Déformation et interactions fluide-roche dans la couverture mésozoïque au dessus du décollement de couverture d'Urdach.

Figure 3supp. Le manteau serpentinisé d'Urdach (échantillon URD4) : aspect microscopique.

Figure 4supp. Les ophicalcites de la carrière de Bilatre (échantillon URD1).

Figure 5supp. Les ophicalcites de la carrière de Bilatre (échantillon URD12).

Figure 6supp. Datations U/Pb in situ sur zircons.

Figure 7supp. Les roches métasomatiques du détachment croûte-manteau.

Figure 8supp. Les roches métasomatiques du décollement de couverture (« ball trap » et Peillou.

Figure 9supp. Les brèches tectoniques triasique de Peillou: échantillon BCOR300c.

Figure 10supp. Les laves dans le flysch de Bilatre : aspects macroscopiques.

549

550 Figure 11supp. Les laves dans le flysch de Bilatre : aspects microscopiques

551

552 Tableau 1. Analyse majeurs et traces de l'échantillon de lave sphérulitique BCOR394d

553 (oxydes wt% et ppm; fer total en Fe_2O_3, LOI (Loss On Ignition): perte au feu à 1050°C.

554 données ICP-AES, Plouzané. Méthode analytique décrite dans Cotten et al. (1995).

555 Tableau 2. Conditions opératoires pour le fonctionnement de l'équipement LA-ICP-MS.

556 Tableau 3. Données U-Th-Pb obtenues sur grains de zircon par LA-ICP-MS

557 Tableaux 4 à 20. Analyses de minéraux à la microsonde : voir conditions analytiques dans

558 le texte principal (en anglais).

559 Tableau 4: Analyses de minéraux à la microsonde de l'échantillon URD9-1

560 Tableau 5: Analyses de minéraux à la microsonde de l'échantillon URD9b

561 Tableau 6: Analyses de minéraux à la microsonde de l'échantillon URD9c

562 Tableau 7: Analyses de minéraux à la microsonde de l'échantillon URD9f

563 Tableau 8: Analyses de minéraux à la microsonde de l'échantillon BCOR115

564 Tableau 9: Analyses de minéraux à la microsonde de l'échantillon URD17b

565 Tableau 10: Analyses de minéraux à la microsonde de l'échantillon URD17a

566 Tableau 11: Analyses de minéraux à la microsonde de l'échantillon URD16

567 Tableau 12: Analyses de minéraux à la microsonde de l'échantillon URD13

568 Tableau 13: Analyses de minéraux à la microsonde de l'échantillon URD18

569 Tableau 14: Analyses de minéraux à la microsonde de l'échantillon URD14

570 Tableau 15: Analyses de minéraux à la microsonde de l'échantillon URD19

571 Tableau 16: Analyses de minéraux à la microsonde de l'échantillon URD15

572 Tableau 17: Analyses de minéraux à la microsonde de l'échantillon BCOR300a

573 Tableau 18: Analyses de minéraux à la microsonde de l'échantillon BCOR300b

574 Tableau 19: Analyses de minéraux à la microsonde de l'échantillon BCOR300c

575 Tableau 20: Analyses de minéraux à la microsonde de l'échantillon BCOR300e

576